

Measurement of $R = \sigma_L/\sigma_T$ in Deep-Inelastic Scattering on Nuclei

A. Airapetian,³¹ N. Akopov,³¹ Z. Akopov,³¹ M. Amarian,^{26,31} V.V. Ammosov,²⁴ E.C. Aschenauer,⁶ R. Avakian,³¹ A. Avetissian,³¹ E. Avetissian,³¹ P. Bailey,¹⁵ V. Baturin,²³ C. Baumgarten,²¹ M. Beckmann,⁵ S. Belostotski,²³ S. Bernreuther,²⁹ N. Bianchi,¹⁰ H.P. Blok,^{22,30} H. Böttcher,⁶ A. Borissov,¹⁹ O. Bouhali,²² M. Bouwhuis,¹⁵ J. Brack,⁴ S. Brauksiepe,¹¹ A. Brüll,¹⁸ I. Brunn,⁸ G.P. Capitani,¹⁰ H.C. Chiang,¹⁵ G. Ciullo,⁹ G.R. Court,¹⁶ P.F. Dalpiaz,⁹ R. De Leo,³ L. De Nardo,¹ E. De Sanctis,¹⁰ E. Devitsin,²⁰ P.K.A. de Witt Huberts,²² P. Di Nezza,¹⁰ M. Düren,¹³ M. Ehrenfried,⁶ A. Elalaoui-Moulay,² G. Elbakian,³¹ F. Ellinghaus,⁶ U. Elschenbroich,¹¹ J. Ely,⁴ R. Fabbri,⁹ A. Fantoni,¹⁰ A. Fechtchenko,⁷ L. Felawka,²⁸ H. Fischer,¹¹ B. Fox,⁴ J. Franz,¹¹ S. Frullani,²⁶ Y. Gärber,⁸ G. Gapienko,²⁴ V. Gapienko,²⁴ F. Garibaldi,²⁶ E. Garutti,²² G. Gavrillov,²³ V. Gharibyan,³¹ G. Graw,²¹ O. Grebenioug,²³ P.W. Green,^{1,28} L.G. Greeniaus,^{1,28} A. Gute,⁸ W. Haeberli,¹⁷ K. Hafidi,² M. Hartig,²⁸ D. Hasch,¹⁰ D. Heesbeen,²² F.H. Heinsius,¹¹ M. Henoeh,⁸ R. Hertenberger,²¹ W.H.A. Hesselink,^{22,30} Y. Holler,⁵ B. Hommez,¹² G. Iarygin,⁷ A. Izotov,²³ H.E. Jackson,² A. Jgoun,²³ R. Kaiser,¹⁴ E. Kinney,⁴ A. Kisselev,²³ P. Kitching,¹ K. Königsmann,¹¹ H. Kolster,¹⁸ M. Kopytin,²³ V. Korotkov,⁶ E. Kotik,¹ V. Kozlov,²⁰ B. Krauss,⁸ V.G. Krivokhijine,⁷ L. Lagamba,³ L. Lapikás,²² A. Laziev,^{22,30} P. Lenisa,⁹ P. Liebing,⁶ T. Lindemann,⁵ W. Lorenzon,¹⁹ N.C.R. Makins,¹⁵ H. Marukyan,³¹ F. Masoli,⁹ F. Menden,¹¹ V. Mexner,²² N. Meyners,⁵ O. Mikloukho,²³ C.A. Miller,^{1,28} V. Muccifora,¹⁰ A. Nagaitsev,⁷ E. Nappi,³ Y. Naryshkin,²³ A. Nass,⁸ K. Negodaeva,⁶ W.-D. Nowak,⁶ K. Oganessyan,^{5,10} H. Ohsuga,²⁹ G. Orlandi,²⁶ S. Podiatchev,⁸ S. Potashov,²⁰ D.H. Potterveld,² M. Raitchel,⁸ D. Reggiani,⁹ P. Reimer,² A. Reischl,²² A.R. Reolon,¹⁰ K. Rith,⁸ G. Rosner,¹⁴ A. Rostomyan,³¹ D. Ryckbosch,¹² Y. Sakemi,²⁹ I. Sanjiev,^{2,23} F. Sato,²⁹ I. Savin,⁷ C. Scarlett,¹⁹ A. Schäfer,²⁵ C. Schill,¹¹ G. Schnell,⁶ K.P. Schüller,⁵ A. Schwind,⁶ J. Seibert,¹¹ B. Seitz,¹ R. Shandize,⁸ T.-A. Shibata,²⁹ V. Shutov,⁷ M.C. Simani,^{22,30} K. Sinram,⁵ M. Stancari,⁹ M. Statera,⁹ E. Steffens,⁸ J.J.M. Steijger,²² J. Stewart,⁶ U. Stösslein,⁴ K. Suetsugu,²⁹ H. Tanaka,²⁹ S. Taroian,³¹ A. Terkulov,²⁰ S. Tessarin,⁹ E. Thomas,¹⁰ A. Tkabladze,⁶ M. Tytgat,¹² G.M. Urciuoli,²⁶ G. van der Steenhoven,²² R. van de Vyver,¹² M.C. Vetterli,^{27,28} V. Vikhrov,²³ M.G. Vincter,¹ J. Visser,²² J. Volmer,⁶ C. Weiskopf,⁸ J. Wendland,^{27,28} J. Wilbert,⁸ T. Wise,¹⁷ S. Yen,²⁸ S. Yoneyama,²⁹ B. Zihlmann,^{22,30} and H. Zohrabian³¹

(The HERMES Collaboration)

¹Department of Physics, University of Alberta, Edmonton, Alberta T6G 2J1, Canada

²Physics Division, Argonne National Laboratory, Argonne, Illinois 60439-4843, USA

³Istituto Nazionale di Fisica Nucleare, Sezione di Bari, 70124 Bari, Italy

⁴Nuclear Physics Laboratory, University of Colorado, Boulder, Colorado 80309-0446, USA

⁵DESY, Deutsches Elektronen-Synchrotron, 22603 Hamburg, Germany

⁶DESY Zeuthen, 15738 Zeuthen, Germany

⁷Joint Institute for Nuclear Research, 141980 Dubna, Russia

⁸Physikalisches Institut, Universität Erlangen-Nürnberg, 91058 Erlangen, Germany

⁹Istituto Nazionale di Fisica Nucleare, Sezione di Ferrara and

Dipartimento di Fisica, Università di Ferrara, 44100 Ferrara, Italy

¹⁰Istituto Nazionale di Fisica Nucleare, Laboratori Nazionali di Frascati, 00044 Frascati, Italy

¹¹Fakultät für Physik, Universität Freiburg, 79104 Freiburg, Germany

¹²Department of Subatomic and Radiation Physics, University of Gent, 9000 Gent, Belgium

¹³Physikalisches Institut, Universität Gießen, 35392 Gießen, Germany

¹⁴Department of Physics and Astronomy, University of Glasgow, Glasgow G12 8QQ, United Kingdom

¹⁵Department of Physics, University of Illinois, Urbana, Illinois 61801, USA

¹⁶Physics Department, University of Liverpool, Liverpool L69 7ZE, United Kingdom

¹⁷Department of Physics, University of Wisconsin-Madison, Madison, Wisconsin 53706, USA

¹⁸Laboratory for Nuclear Science, Massachusetts Institute of Technology, Cambridge, Massachusetts 02139, USA

¹⁹Randall Laboratory of Physics, University of Michigan, Ann Arbor, Michigan 48109-1120, USA

²⁰Lebedev Physical Institute, 117924 Moscow, Russia

²¹Sektion Physik, Universität München, 85748 Garching, Germany

²²Nationaal Instituut voor Kernfysica en Hoge-Energiefysica (NIKHEF), 1009 DB Amsterdam, The Netherlands

²³Petersburg Nuclear Physics Institute, St. Petersburg, Gatchina, 188350 Russia

²⁴Institute for High Energy Physics, Protvino, Moscow oblast, 142284 Russia

²⁵Institut für Theoretische Physik, Universität Regensburg, 93040 Regensburg, Germany

²⁶Istituto Nazionale di Fisica Nucleare, Sezione Roma 1, Gruppo Sanità

and Physics Laboratory, Istituto Superiore di Sanità, 00161 Roma, Italy

²⁷Department of Physics, Simon Fraser University, Burnaby, British Columbia V5A 1S6, Canada

²⁸TRIUMF, Vancouver, British Columbia V6T 2A3, Canada

²⁹Department of Physics, Tokyo Institute of Technology, Tokyo 152, Japan

³⁰Department of Physics and Astronomy, Vrije Universiteit, 1081 HV Amsterdam, The Netherlands

³¹Yerevan Physics Institute, 375036 Yerevan, Armenia

(Dated: June 19, 2002)

Cross section ratios for deep-inelastic scattering from ${}^3\text{He}$, ${}^{14}\text{N}$ and ${}^{84}\text{Kr}$ with respect to ${}^2\text{H}$ have been measured by the HERMES collaboration at DESY using a 27.5 GeV positron beam. The data cover a range in the Bjorken scaling variable x between 0.010 and 0.65, the negative squared four-momentum transfer Q^2 varies from 0.5 to 15 GeV², while at small values of x and Q^2 , the virtual photon polarisation parameter ϵ extends to lower values than previous measurements. From the dependence of the data on ϵ , values for R_A/R_D with R the ratio σ_L/σ_T of longitudinal to transverse DIS cross sections have been derived and found to be consistent with unity.

The multi-GeV energy scale at which deep-inelastic scattering (DIS) is typically employed to study the partonic structure of nucleons greatly differs from the multi-MeV scale relevant to the atomic nucleus. Hence, it came as a surprise that the nucleon structure function $F_2(x)$ was found to depend on the mass A of the atomic nucleus [1], indicating that the quark momentum distributions in bound nucleons differ from those in free nucleons. This phenomenon is known as the *EMC effect* at large values of the Bjorken scaling variable x ($x > 0.1$), and as *shadowing* at lower values of x [2].

With $F_2(x)$ found to be A -dependent, it is relevant to investigate whether this dependence is the same for its longitudinal and transverse components, $F_L(x)$ and $F_1(x)$. The latter two structure functions are related to $F_2(x)$ via $F_L(x) = (1 + Q^2/\nu^2)F_2(x) - 2xF_1(x)$ with $-Q^2$ the square of the four-momentum transfer, ν the energy transfer, $x = Q^2/2M\nu$ and M the nucleon mass. A possible difference between the A -dependences of $F_L(x)$ and $F_1(x)$ can be investigated by measuring the ratio of longitudinal to transverse deep-inelastic scattering cross sections $R = \sigma_L/\sigma_T = F_L(x)/2xF_1(x)$ for various nuclear targets. While several such studies have been reported [28–30], none of these has provided values of R in the kinematic regime $x < 0.06$ with $Q^2 < 1$ GeV². This region is the focus of the present paper.

In deep-inelastic charged lepton scattering from an unpolarised target, the double-differential cross section per nucleon can be written in the one-photon exchange approximation as

$$\begin{aligned} \frac{d^2\sigma}{dx dQ^2} &= \frac{4\pi\alpha^2}{Q^4} \frac{F_2(x, Q^2)}{x} \times \\ &\left[1 - y - \frac{Q^2}{4E^2} + \frac{y^2}{2} \left(\frac{1 + Q^2/\nu^2}{1 + R(x, Q^2)} \right) \right] \\ &= \frac{\sigma_{\text{Mott}}}{E'E} \frac{\pi F_2(x, Q^2)}{x\epsilon} \frac{1 + \epsilon R(x, Q^2)}{1 + R(x, Q^2)}, \end{aligned} \quad (1)$$

where $y = \nu/E$, σ_{Mott} represents the cross section for lepton scattering from a point charge, and E and E' are

the initial and final lepton energies, respectively. The virtual photon polarisation parameter is given by

$$\epsilon = \frac{4(1-y) - Q^2/E^2}{4(1-y) + 2y^2 + Q^2/E^2}. \quad (2)$$

The ratio of DIS cross sections on nucleus A and deuterium D ($={}^2\text{H}$) is then given by:

$$\frac{\sigma_A}{\sigma_D} = \frac{F_2^A (1 + \epsilon R_A)(1 + R_D)}{F_2^D (1 + R_A)(1 + \epsilon R_D)}, \quad (3)$$

where R_A and R_D represent the ratio σ_L/σ_T for nucleus A and deuterium. To facilitate easier interpretation and in accordance to the literature, here and throughout this paper all cross sections are defined as cross sections per nucleon and are converted to cross sections for isoscalar nuclei, i.e. the measured cross sections are divided by the atomic number A and corrected for any difference in the number of protons and neutrons:

$$\frac{\sigma_A}{\sigma_D} \equiv \frac{\sigma_A^{\text{nucleus}}}{Z\sigma_p + (A-Z)\sigma_n}, \quad (4)$$

where $\sigma_A^{\text{nucleus}}$ is the DIS cross section per atom for nucleus A and σ_p and σ_n are the DIS cross sections on the proton and the neutron. In practice, $\sigma_A^{\text{nucleus}}/\sigma_D$ is converted to σ_A/σ_D using the known cross section ratio σ^D/σ^p [3].

For $\epsilon \rightarrow 1$ the cross section ratio equals the ratio of structure functions F_2^A/F_2^D . For smaller values of ϵ the cross section ratio is equal to F_2^A/F_2^D only if $R_A = R_D$. A difference between R_A and R_D will thus introduce an ϵ -dependence of σ_A/σ_D . Hence, measurements of σ_A/σ_D as a function of ϵ can be used to extract experimental information on R_A/R_D , if R_D is known.

In this paper we present data from the HERMES experiment on the cross section ratio for deep-inelastic positron scattering off helium-3, nitrogen and krypton with respect to deuterium. The helium-3 and nitrogen data were published in a previous letter [4]. Recently,

those data were found to be subject to an A-dependent tracking inefficiency of the HERMES spectrometer [5], which was not recognised in the previous analysis. The resulting correction of the cross section ratios is significant at low values of x and Q^2 and substantially changes the interpretation of those data. The data presented here were corrected for this effect and supersede those published in Ref. [4].

The data were collected by the HERMES experiment at DESY using ^1H , ^2H , ^3He , ^{14}N and ^{84}Kr molecular gas targets internal to the 27.5 GeV positron storage ring of HERA. The target gases were injected into a 40 cm long, tubular open-ended storage cell inside the positron ring. The luminosity was measured by detecting Bhabha-scattered target electrons in coincidence with the scattered positrons, in a pair of $\text{NaBi}(\text{WO}_4)_2$ electromagnetic calorimeters.

The HERMES spectrometer [6] is a forward angle instrument which is symmetric about a central horizontal shielding plate in the magnet. Both the scattered positrons and the hadrons produced can be detected and identified within an angular acceptance of ± 170 mrad horizontally, and 40 – 140 mrad vertically. The trigger was formed from a coincidence between signals of three scintillator hodoscope planes and a lead-glass calorimeter where a minimum energy deposit of 3.5 GeV was required. Positron identification was accomplished using the calorimeter, the second hodoscope, which functioned as a preshower counter, a transition-radiation detector and a Čerenkov counter. This system provided positron identification with an average efficiency of 99 % and a hadron contamination of less than 1 %.

Deep-inelastic scattering events were extracted from the data by imposing constraints on Q^2 ($Q^2 > 0.3 \text{ GeV}^2$), W (the invariant mass of the photon-nucleon system, required to be greater than 2 GeV), and y ($y < 0.85$). At very low x and high y , the nuclear cross sections are dominated by radiative processes associated with elastic scattering. To limit these contributions, a minimum x value of $x = 0.01$ was required.

As the ratio σ_A/σ_D involves nuclei with different numbers of protons, radiative corrections do not cancel in the ratio. In particular, the yield of radiative processes associated with elastic scattering scales with Z^2 and thus differs for the two target nuclei. At small values of apparent x and Q^2 (inferred from the kinematics of the scattered positron), corresponding to large values of y , the contribution from radiative elastic scattering becomes large. In this kinematic region, the associated energetic photons radiated at small angles can produce electromagnetic showers that cause large tracking inefficiencies [5]. Corrections for these process-specific inefficiencies must be applied, since they increase in severity as the Z of nuclear targets increases.

These track reconstruction losses in the HERMES de-

tor have been simulated in detail using the GEANT-based Monte Carlo description of the experiment. The probability of photon emission is modelled following the description of Mo and Tsai [7], and has been carefully compared to other calculations of radiative processes. All materials close to the beam pipe have been implemented in detail and the effect of the minimum energy of the secondary particles tracked through the detector was investigated. The resulting reconstruction losses at low x and Q^2 strongly depend on the target material and show a strong variation with y , and consequently with x and Q^2 . The ratios of the reconstruction efficiencies η for target nucleus A compared to deuterium are shown in Fig. 1 as a function of x , for the various target materials used in the HERMES experiment. For completeness, this figure includes points at smaller values of x than are employed in the present analysis.

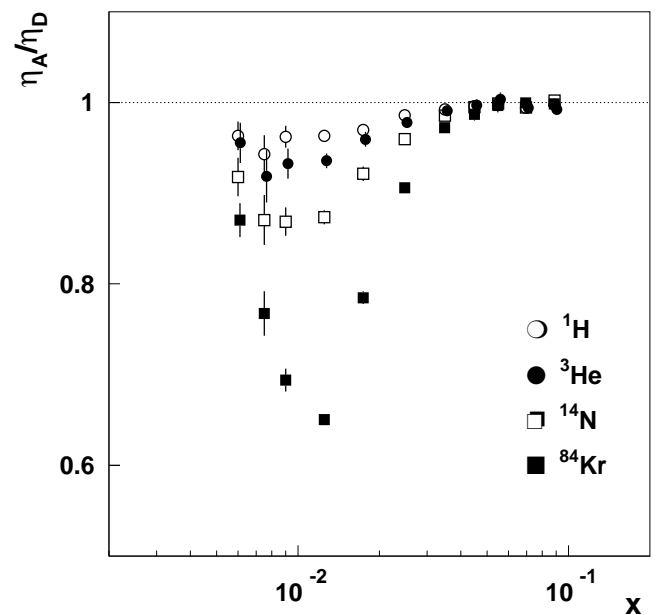


FIG. 1: Ratio of track reconstruction efficiencies in ^1H , ^3He , ^{14}N and ^{84}Kr with respect to ^2H as function of x .

The systematic uncertainty of this correction was estimated using the fact that the HERMES spectrometer consists of two independent detectors above and below the positron beam. For about 50 % of the events with a hard radiated photon the resulting electromagnetic shower is contained in one detector while the scattered electron is found in the other detector. While these events are rejected by the standard HERMES reconstruction algorithm because of their high total multiplicity, they can be reconstructed when one considers the two detectors independently. The number of events gained in this way strongly depends on the details of the electromagnetic shower – especially on the energy of the ra-

diated photon and the exact position where the photon hits any material – and thus provides a good measure of the quality of the MC simulation. Reasonable agreement between the data and the simulation is found for all target materials. Fig. 2 shows as a function of apparent x the fractional change in the yield ratios when treating the upper and lower spectrometer halves independently, both for the data and the MC simulation. Here the yields from the two detector halves have been averaged. A difference between the yields in the upper and the lower detector observed in the data is attributed to a relative misalignment between the two detectors and is included in the statistical uncertainty by scaling the error with the square root of χ^2 , calculated from the probability that both measurements are consistent. This difference between the yields in the two detectors is significant only in the krypton data at low x ($x < 0.03$) where the reconstruction efficiency quickly changes with x and the difference can be up to 10 %. The difference between the data and the MC simulation is treated as a systematic uncertainty.

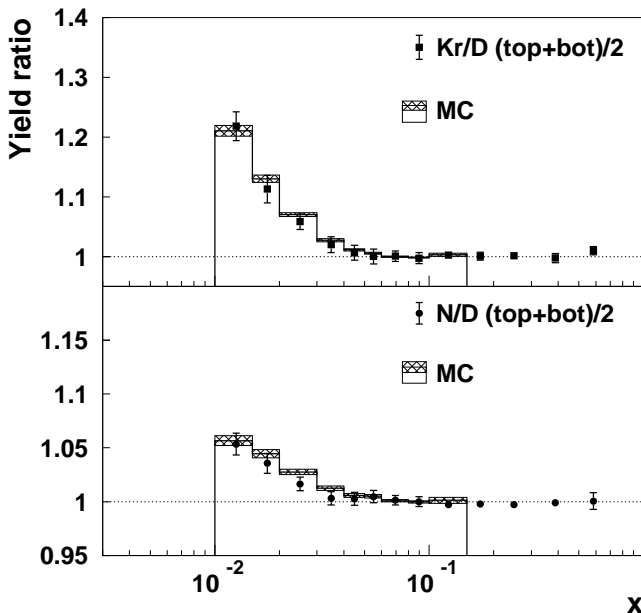


FIG. 2: Comparison between data (points) and MC simulation (histogram) for the fractional change in the cross section ratios when treating the upper and lower HERMES detector halves independently.

After the correction for the reconstruction inefficiencies, the data have to be corrected for radiative processes. These have been computed using the method outlined in Ref. [8]. For the evaluation of the coherent radiative tails, the nuclear elastic form factors must be known. Parameterisations of the form factors of ^2H , ^3He , ^{14}N and ^{84}Kr were taken from the literature [9–12]. For the quasi-elastic tails, the nucleon form factor parameterisation of

Gari and Krümpelmann [13] was used. The reduction of the bound nucleon cross section with respect to the free nucleon one (quasi-elastic suppression) was evaluated using the results of a calculation by Bernabeu [14] for deuterium and the non-relativistic Fermi gas model for ^3He , ^{14}N and ^{84}Kr [15]. The evaluation of the inelastic QED processes requires the knowledge of both F_2 and R over a wide range of x and Q^2 . The structure function $F_2^D(x, Q^2)$ was described by a Regge motivated parameterisation of the proton structure function $F_2^p(x, Q^2)$ [16] multiplied by the NMC measurement of F_2^D/F_2^p [3]; for R_D the Whitlow parameterisation [17] was used. The nuclear structure functions $F_2^A(x, Q^2)$ were taken from phenomenological fits to the SLAC and NMC data, and $R_A(x, Q^2)$ was assumed to be equal to $R_D(x, Q^2)$. The effects of all radiative processes were subtracted from the measured yields and the statistical errors propagated accordingly. This method avoids the possible large model dependence that can result from multiplicatively applying radiative corrections [18].

For high- Z targets such as krypton, the probability for the exchange of more than one photon becomes non-negligible. The corresponding amplitudes lead to a destructive interference with the leading amplitudes. For the dominant contribution to the radiative corrections — the coherent radiative tail — this effect has been estimated using the distorted wave function method [19], resulting into a 5–10 % reduction of the radiative elastic tail. Other contributions proportional to $Z \cdot \alpha_{EM}$ might be non-negligible but could not be estimated.

The size of the radiative corrections is largest in the lowest x -bin ($x = 0.0125, y = 0.77$), where the correction, expressed as an over-all factor, amounts to 0.57, 0.50, 0.46, and 0.31 for ^2H , ^3He , ^{14}N , and ^{84}Kr , respectively. The systematic uncertainty in the radiative corrections was estimated by using upper and lower limits of the parameterisations, or alternative parameterisations [17, 20–22] for all the above input parameters. The resulting systematic uncertainty in the cross section ratio of Kr/D is about 6 % at low x , quickly falling to values smaller than 1 % for $x > 0.06$. (As mentioned before this uncertainty does not include the effects of multiphoton exchange (Coulomb distortion) beyond the estimated contribution to the coherent elastic tail; these contributions might be non-negligible but could not be estimated.) Because of the smaller radiative contributions, the uncertainties due to the radiative corrections in the cross section ratios of nitrogen and helium with respect to deuterium are about 3 % at low x .

The effects originating from the finite resolution of the spectrometer and from the hadron contamination in the positron sample have been determined and found to be negligible. The overall normalisation uncertainty has been estimated from the luminosity measurements to be 1.8 % for the He(N)/D data and 1 % for the Kr/D data.

The results of the present analysis [23] are shown in Fig. 3 as a function of x . Also shown are the results of the NMC [24–26] and SLAC [27] measurements of σ_{He}/σ_D , σ_C/σ_D and σ_{Sn}/σ_D where the NMC values for σ_{Sn}/σ_D have been obtained from the measurements of σ_{Sn}/σ_C and σ_C/σ_D . On average, the present data on σ_{He}/σ_D and σ_N/σ_D are about 1.5 % below the cross section ratio reported by NMC. A similar difference is observed in comparison to the SLAC data which cover a smaller x but the same Q^2 range than the HERMES data. As the normalisation uncertainty of the present data is considerably larger than that of the NMC data (0.4 %), the σ_{He}/σ_D and σ_N/σ_D results have been renormalised by 1.5 %. No such renormalisation has been applied to the Kr/D cross section ratios. For x values below $x = 0.1$, the present data on N/D and Kr/D are slightly below the NMC data but consistent within the present statistical and systematic uncertainties.

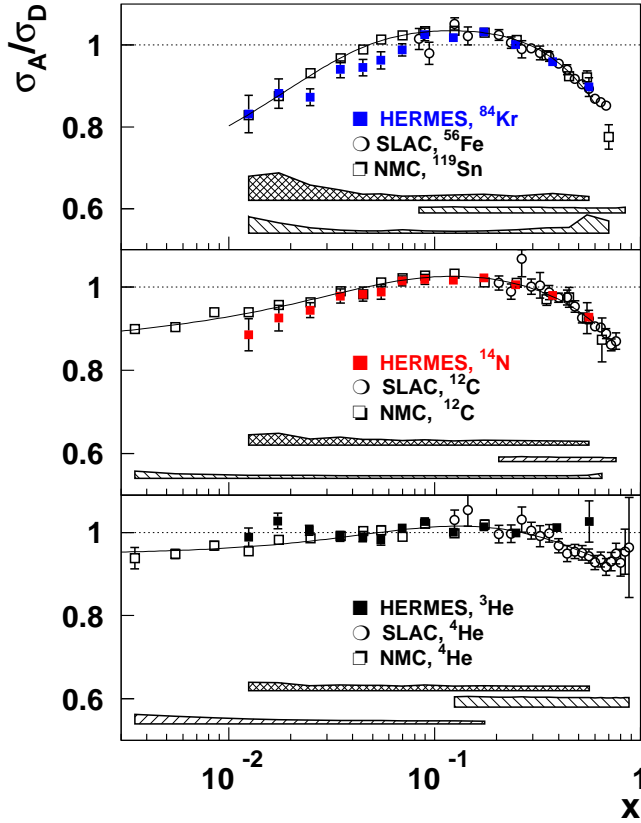


FIG. 3: Ratio of isoscalar Born cross sections of inclusive deep-inelastic lepton scattering from nucleus A and D versus x . The error bars represent the statistical uncertainties, the systematic uncertainties are given by the error bands (ordered as HERMES, SLAC, NMC). The HERMES ${}^3\text{He}/D$ and ${}^{14}\text{N}/D$ data have been renormalised by 1.5 %.

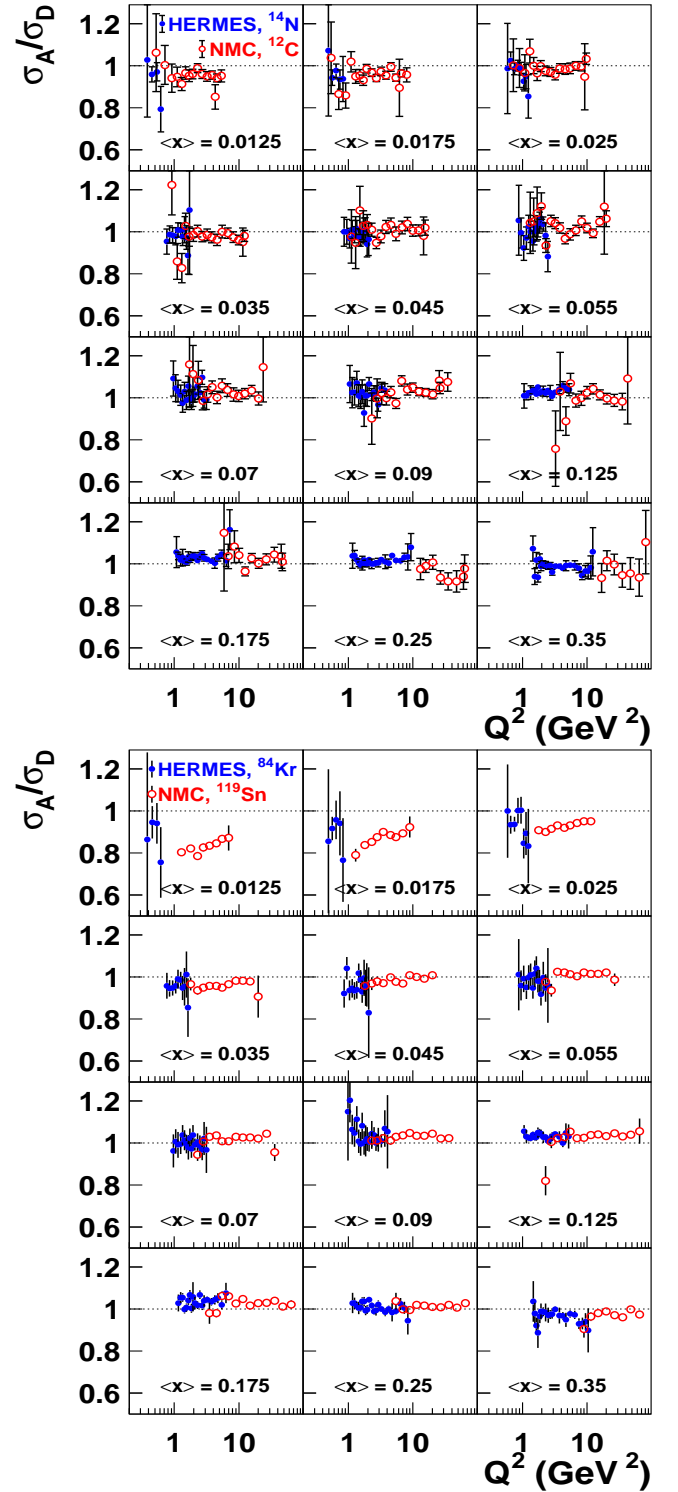


FIG. 4: Ratio of isoscalar Born cross sections of inclusive deep-inelastic lepton scattering from nucleus A and D as function of Q^2 for fixed values of x . The error bars represent the statistical uncertainties. The HERMES ${}^3\text{He}/D$ and ${}^{14}\text{N}/D$ data have been renormalised by 1.5 %.